FUNCTIONAL NEURORADIOLOGY

MR imaging differentiation of Fe^{2+} and Fe^{3+} based on relaxation and magnetic susceptibility properties

Olaf Dietrich[1] · Johannes Levin[2,3] · Seyed-Ahmad Ahmadi[2] · Annika Plate[2] ·
Maximilian F. Reiser[4] · Kai Bötzel[2] · Armin Giese[5] · Birgit Ertl-Wagner[4]

Abstract

Purpose The aim of this study is to evaluate the MR imaging behavior of ferrous (Fe^{2+}) and ferric (Fe^{3+}) iron ions in order to develop a noninvasive technique to quantitatively differentiate between both forms of iron.

Methods MRI was performed at 3 T in a phantom consisting of 21 samples with different concentrations of ferrous and ferric chloride solutions (between 0 and 10 mmol/L). A multi-echo spoiled gradient-echo pulse sequence with eight echoes was used for both T_2^* and quantitative susceptibility measurements. The transverse relaxation rate, $R_2^* = 1/T_2^*$, was determined by nonlinear exponential fitting based on the mean signals in each sample. The susceptibilities, χ, of the samples were calculated after phase unwrapping and background field removal by fitting the spatial convolution of a unit dipole response to the measured internal field map. Relaxation rate changes, $\Delta R_2^*(c_{Fe})$, and susceptibility changes, $\Delta\chi(c_{Fe})$, their linear slopes, as well as the ratios $\Delta R_2^*(c_{Fe}) / \Delta\chi(c_{Fe})$ were determined for all concentrations.

Results The linear slopes of the relaxation rate were (12.5 ± 0.4) $s^{-1}/(mmol/L)$ for Fe^{3+} and (0.77 ± 0.09) $s^{-1}/(mmol/L)$ for Fe^{2+} (significantly different, z test $P < 0.0001$). The linear slopes of the susceptibility were (0.088 ± 0.003) ppm/(mmol/L) for Fe^{3+} and (0.079 ± 0.006) ppm/(mmol/L) for Fe^{2+}. The individual ratios $\Delta R_2^*/\Delta\chi$ were greater than 40 s^{-1}/ppm for all samples with ferric solution and lower than 20 s^{-1}/ppm for all but one of the samples with ferrous solution.

Conclusion Ferrous and ferric iron ions show significantly different relaxation behaviors in MRI but similar susceptibility patterns. These properties can be used to differentiate ferrous and ferric samples.

Keywords Magnetic resonance imaging · Iron · Ferric and ferrous chloride · Relaxation · Magnetic susceptibility

OD and JL contributed equally to this study.

✉ Olaf Dietrich
   od@dtrx.net

1 Josef Lissner Laboratory for Biomedical Imaging, Institute for Clinical Radiology, Ludwig-Maximilians-University Hospital Munich, Marchioninistr. 15, 81377 Munich, Germany

2 Department of Neurology, Ludwig-Maximilians-University Hospital Munich, Munich, Germany

3 German Center for Neurodegenerative Diseases (DZNE), Munich, Germany

4 Institute for Clinical Radiology, Ludwig-Maximilians-University Hospital Munich, Munich, Germany

5 Center for Neuropathology and Prion Research, Ludwig-Maximilians-University Munich, Munich, Germany

Introduction

Iron homeostasis is a decisively important factor in maintaining the physiological functioning of the brain [1]. Using magnetic resonance imaging (MRI), iron can be visualized and measured by quantitative susceptibility mapping (QSM) techniques, which quantify magnetic susceptibility sources. Brain iron mapping with QSM has increasingly been in the focus of clinical attention in recent years, as increased iron levels have been described in patients with Parkinson's disease (PD) [2], in the motor cortex of patients suffering from amyotrophic lateral sclerosis [3], as well as in the basal ganglia of patients with Huntington's chorea [4].

A potential dysregulation of iron metabolism with subsequent alterations of the iron concentration has been implied as a potential factor or cofactor in neurodegenerative diseases such as dementia of the Alzheimer's type (AD) and PD as well as in neuroinflammatory disorders such as multiple sclerosis [5–7]. For example, in the pathogenesis of PD, a strong line of evidence indicates a pivotal role of iron ions [8]. This is based on data from in vitro studies [9, 10], animal experiments [11], and human epidemiological and in vivo research [12, 13]. However, an increase in iron concentration in some regions of the brain is also viewed as a feature of normal aging [14, 15]. Interestingly, postmortem analysis of human brain tissue shows not only an increase in iron content in the affected brain areas but also a shift of the ratio of ferrous (Fe^{2+}) to ferric iron ions (Fe^{3+}) towards an increased content in ferric iron ions [16]. Whether iron is present in its ferric or ferrous form may have important implications for its biological effect and it would be desirable to noninvasively differentiate these forms in the brain in the in vivo situation.

The presence of iron in a sample or in tissue can be detected with MRI by relaxation-based methods [17–20] or by susceptibility-sensitive techniques [17, 19, 21–24]. Both approaches have been used for quantitative estimations of tissue iron concentrations. A wide range of slopes describing the linear dependence of relaxation rates and iron concentrations in brain tissue have been published (see Table 5 in ref. [17] for a review). However, these dependencies for iron-induced relaxation changes were determined in most cases without considering differences between the relaxivities of the ferric and ferrous form of stored iron [25–27].

The purpose of the present study is therefore to evaluate the MR imaging behavior of ferrous and ferric iron ions in order to develop a noninvasive technique to quantitatively differentiate between both forms of iron.

Methods

A phantom was built consisting of 21 cylindrical tubes (diameter 10 mm, length 40 mm) with different concentrations (0.0, 0.1, 0.3, 1.0, 3.0, and 10 mmol/L) of ferrous ($FeCl_2$) and ferric ($FeCl_3$) chloride solutions (Merck, Darmstadt, Germany); the solvent was purified water (H_2O Millipore). Furthermore, four concentrations (0.0, 0.1, 1.0, 10.0 mmol/L) of ferric chloride were prepared with additional hydrochloric acid (HCl, pH = 2; Roth, Karlsruhe, Germany) since HCl suppresses the formation of $Fe(OH)_3$, which is poorly soluble in water and would therefore precipitate. Four concentrations (0.0, 0.1, 1.0, 10.0 mmol/L) of ferrous chloride were prepared with sodium ascorbate (NaAsc, 10 mmol/L, Roth, Karlsruhe, Germany) since ascorbate suppresses the oxidation of unstable Fe^{2+} ions to Fe^{3+}. Finally, one sample contained deferoxamine (10 mmol/L, Sigma-Aldrich, Munich, Germany) and one

sample 1.0 mmol/L ferric chloride with deferoxamine, which chelates iron. All 21 tubes were positioned in an approximately rectangular box of size $200 \times 100 \times 55$ mm^3 molded with a polyvinyl alcohol cryogel (PVAc) [28, 29] (compare Fig. 1a). PVAc was transferred into its solid state via one freeze–thaw cycle and then stored at 4 °C. Before the measurements, the phantom was kept at room temperature (20 °C) for at least 4 h such that all 40-mL samples could reach room temperature.
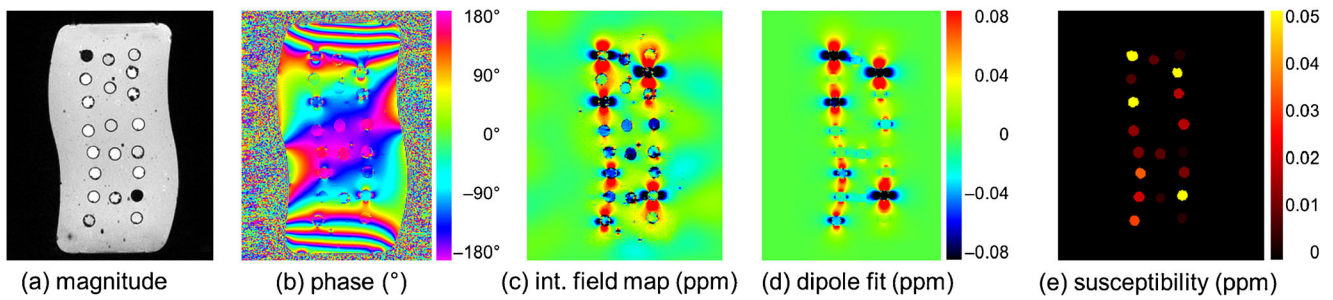
The phantom was examined on a 3-T whole-body MRI system (Magnetom Verio, Siemens Healthcare, Erlangen, Germany) equipped with a 12-channel head coil. A multi-echo spoiled gradient-echo pulse sequence with eight echoes was used for both T_2^* and quantitative susceptibility measurements. The echo times were TE = 10, 20, 30, 40, 50, 60, 70, and 80 ms (with monopolar/"flyback" readout) at a repetition time of TR = 95 ms; the flip angle was 20°. Magnitude and phase data (Fig. 1a, b) were acquired in coronal orientation with a matrix size of $320 \times 260 \times 40$ voxels and a voxel size of $0.72 \times 0.72 \times 1.40$ mm^3; the receiver bandwidth was 130 Hz/pixel.

For evaluation, each sample tube was manually segmented in all slices, resulting in 21 volumes of interests (VOI). Quantitative evaluation was restricted to six central slices (slice numbers 20 to 25 from 40), which showed the lowest levels of artifacts due to field inhomogeneity.

The transverse relaxation rate, $R_2^* = 1/T_2^*$, was determined by nonlinear exponential fitting ($S\,(\text{TE}) = S_0 \exp\left(-R_2^* \cdot \text{TE}\right)$) based on the mean signals, $S(\text{TE})$, of all eight echoes in each slice and each sample; then, the mean value and the standard deviation of R_2^* over the six evaluated slices were calculated (thus, allowing an estimation of the variability of the calculated values).

The susceptibilities, χ, of the samples were calculated separately for the acquisitions with TE = 10, 20, and 30 ms, since phase data at longer TEs showed high levels of artifacts. First, the acquired phase data were unwrapped using the "best path" 3D phase unwrapping algorithm [30]. The "Sophisticated Harmonic Artifact Reduction for Phase data" (SHARP) algorithm [31, 32] was applied to the unwrapped phase data for background field removal (with a kernel radius of 6 mm and a regularization parameter of 0.05), resulting in (internal) field maps $\phi(\boldsymbol{r}; \text{TE})$ for each of the three echo times based on the sample susceptibilities only (Fig. 1c). Then, the magnetic unit dipole response with a kernel size of $103 \times 103 \times 53$ pixels was numerically convolved with the shape of each individual sample tube (i.e., each segmented VOI), resulting in 21 spatial field distributions $f_n(\boldsymbol{r})$, $n = 1, \ldots, 21$. Finally, 21 susceptibility coefficients χ_n were determined for each evaluated slice Slc(k) using nonlinear least-squares optimization to fit the superposition of the 21 field distributions to the measured internal field map:

$$\{\chi_n\}_{n=1\ldots21} = \arg\min_{\{\chi_n\}} \sum_{\boldsymbol{r}\in \text{Slc}(k)} \left(\phi(\boldsymbol{r}; \text{TE}) - \sum_{n=1}^{21} \chi_n f_n(\boldsymbol{r})\right)^2.$$

(a) magnitude (b) phase (°) (c) int. field map (ppm) (d) dipole fit (ppm) (e) susceptibility (ppm)

Fig. 1 Phantom with 21 samples and post-processing steps of quantification of magnetic susceptibility. **a** Magnitude data of a central slice (slice number 23 of 40) of the phantom. **b** Phase data of the same slice. **c** Internal magnetic field perturbations determined with the SHARP algorithm. **d** Dipole fit to the field map. **e** Map visualization of calculated magnetic susceptibility distribution

(i.e., the difference between measurement $\phi(\boldsymbol{r}; TE)$ and model was minimized simultaneously for all pixels $\boldsymbol{r} \in \mathrm{Slc}(k)$ in slice number k.) This procedure, which was similar to an approach proposed by de Rochefort et al. [33], resulted in 18 sets (6 slices × 3 echo times) of 21 susceptibility values (Fig. 1d, e); each susceptibility was averaged over all slices and echo times (with calculation of the standard deviation).

To analyze the different behaviors of ferrous and ferric chloride solutions, we determined the relaxation rate changes $\Delta R_2^*(c_{Fe}) = R_2^*(c_{Fe}) - R_2^*(c_{Fe} = 0)$ and the susceptibility changes $\Delta\chi(c_{Fe}) = \chi(c_{Fe}) - \chi(c_{Fe} = 0)$ for all concentrations, since (ferric or ferrous) ions are expected to influence $\Delta R_2^*(c_{Fe})$ and $\Delta\chi(c_{Fe})$ directly proportional to the iron concentration, c_{Fe}. From these difference values, the linear slopes of $\Delta R_2^*(c_{Fe})$ and $\Delta\chi(c_{Fe})$ as functions of the iron concentration were calculated using linear regression analysis; these slopes quantitatively describe the strength of the influence of (ferrous or ferric) ions on relaxation and susceptibility (the slope of $\Delta R_2^*(c_{Fe})$ is simply the relaxivity of ferrous or ferric chloride). Finally, the "relaxation-to-susceptibility" ratio $\Delta R_2^*(c_{Fe}) / \Delta\chi(c_{Fe})$ was calculated for all samples, since this

quantity was hypothesized to differentiate between ferrous and ferric chloride solutions.

For statistical evaluation, the slopes of $\Delta R_2^*(c_{Fe})$ of samples with ferrous and with ferric chloride solutions were compared using the z test [34]; the same comparison was performed for the slopes of $\Delta\chi(c_{Fe})$. We used Fisher's exact test (two-tailed) to evaluate the performance of the relaxation-to-susceptibility ratio $\Delta R_2^*(c_{Fe}) / \Delta\chi(c_{Fe})$ for the differentiation of Fe^{2+} and Fe^{3+}. P values lower than 0.05 were considered to indicate statistically significant differences. All mathematical evaluations were performed with GNU Octave 3.8.2 (<https://gnu.org/software/octave>) and all statistical evaluations were performed with R version 3.1.1 (The R Foundation for Statistical Computing, Vienna, Austria; <http://www.R-project.org>).

Results

The results of all quantitative measurements are listed in Table 1. Overall, we found increasing relaxation rates, R_2^*,

Table 1 Mean values (standard deviations) of relaxation rates (R_2^*) and susceptibilities (χ)

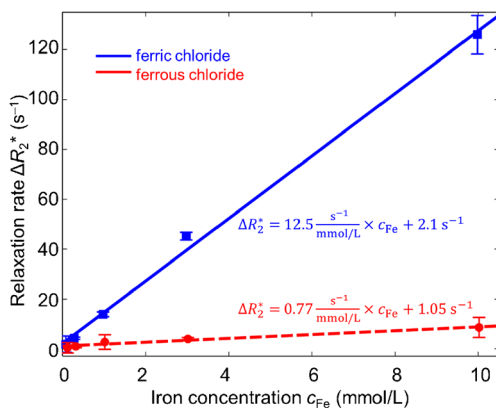|		Iron concentration c_{Fe}					
		0 mmol/L	0.1 mmol/L	0.3 mmol/L	1 mmol/L	3 mmol/L	10 mmol/L
R_2^* (1/s)	Fe^{3+}	0.000 (0.000)	3.180 (3.109)	4.197 (0.456)	11.43 (0.46)	45.2 (1.5)	125.9 (5.5)
	Fe^{3+} Hcl	3.956 (0.681)	4.403 (0.915)	–	20.28 (0.48)	–	130.0 (5.3)
	Fe^{3+} deferox	2.155 (1.133)	–	–	5.12 (0.81)	–	–
	Fe^{2+}	0.000 (0.000)	0.005 (0.012)	0.916 (0.529)	2.80 (0.92)	3.91 (0.56)	7.31 (1.48)
	Fe^{2+} NaAsc	4.784 (1.901)	5.474 (0.854)	–	7.32 (2.06)	–	14.61 (3.25)
χ (ppm)	Fe^{3+}	0.002 (0.010)	−0.005 (0.052)	0.064 (0.043)	0.186 (0.049)	0.342 (0.031)	1.045 (0.161)
	Fe^{3+} Hcl	0.018 (0.036)	0.106 (0.021)	–	0.143 (0.030)	–	0.825 (0.122)
	Fe^{3+} deferox	0.044 (0.027)	–	–	0.113 (0.016)	–	–
	Fe^{2+}	0.002 (0.010)	0.099 (0.042)	0.008 (0.008)	0.195 (0.040)	0.335 (0.023)	0.604 (0.042)
	Fe^{2+} NaAsc	0.142 (0.087)	0.134 (0.076)	–	0.232 (0.033)	–	1.159 (0.041)

Note that this table contains the *absolute* values of the originally measured relaxation rates R_2^* and susceptibilities χ, whereas further evaluation was based on the *changes* ΔR_2^* and $\Delta\chi$ of these quantities relative to the corresponding solutions without iron (but—if applicable—with the same addendum such as HCl or NaAsc) given in the first data column (with $c_{Fe} = 0$ mmol/L)

and susceptibilities, χ, with increasing concentrations of iron. At the highest concentration (10 mmol/L), the relaxation rates increased by about 120–130 s^{-1} for ferric ions and by about 7–10 s^{-1} for ferrous ions (relative to the values at an iron concentration of 0). The susceptibility of both ferric and ferrous ions increased by about 0.6–1.0 ppm at the highest iron concentrations.
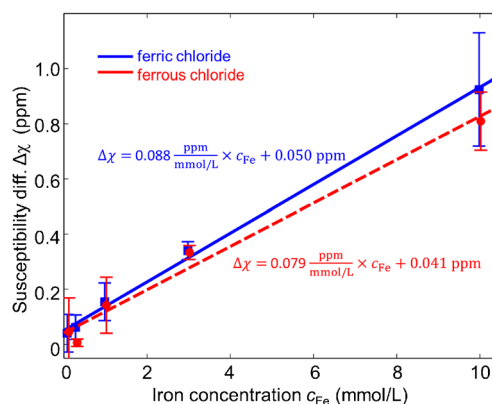
Ferric ions with added HCl behaved very similarly to pure ferric chloride solutions; in contrast, deferoxamine reduced the relaxation rate change at 1 mmol/L ferric ions. Ferrous ions with added sodium ascorbate showed a slightly higher increase of both ΔR_2^* and $\Delta\chi$ at the highest iron concentrations.

To estimate the dependence of the relaxation rate and the susceptibility on the iron concentration quantitatively, we combined the results for Fe^{3+} with and without HCl, and we also combined the results for Fe^{2+} with and without sodium ascorbate; the data combination was performed to reduce the statistical fluctuations of the measured data. With these data, we calculated a linear slope of the relaxation rate of (12.5 ± 0.4) s^{-1}/(mmol/L) for Fe^{3+} and a slope of (0.77 ± 0.09) s^{-1}/(mmol/L) for Fe^{2+}. These two slopes were significantly different ($Z = 26.8$, $P < 0.0001$). The linear slopes of the susceptibility were (0.088 ± 0.003) ppm/(mmol/L) for Fe^{3+} and (0.079 ± 0.006) ppm/(mmol/L) for Fe^{2+}. These slopes were not significantly different ($Z = 1.46$, $P = 0.14$). The combined values of ΔR_2^* and $\Delta\chi$ as well as the calculated slopes are shown in Figs. 2 and 3.

The ratio $\Delta R_2^*/\Delta\chi$ was greater than 40 s^{-1}/ppm for all five concentrations of ferric solution and lower than 20 s^{-1}/ppm for all but one (i.e., for 4) of the concentrations of ferrous solution (the single exception was the concentration of 0.3 mmol/L ferrous chloride, which is displayed as visual outlier in Fig. 4). Using a threshold of 30 s^{-1}/ppm, the sensitivity and specificity of the relaxation-to-susceptibility ratio for the

Fig. 3 Dependence of susceptibility change $\Delta\chi$ on the iron concentration shown for Fe^{3+} (*blue solid line*) and Fe^{2+} (*red dashed line*). *Plotted* data are shown as mean values with standard deviations from evaluations at three different TEs in six slices (and sample combination as described in the "Results" section)

detection of Fe^{2+} were 80% and 100%, respectively, resulting in an accuracy of 90% (Fisher's exact test demonstrated statistical significance with $P = 0.0476$).

Discussion

Our results illustrate a significant difference between the T_2^* relaxivity of ferrous and ferric chloride solution. This difference has previously been analyzed for T_1 and T_2 relaxation times in the context of NMR applications [25] of Fricke gels for radiation dosimetry [27]. The difference is caused by different correlation times of the dipolar interactions between iron ions and water protons; in particular, substantial differences of the electron spin relaxation times are described to be the reason for a much more efficient relaxation process of water protons in the neighborhood of Fe^{3+} than of Fe^{2+} [25,

Fig. 2 Dependence of relaxation rate change ΔR_2^* on the iron concentration shown for Fe^{3+} (*blue solid line*) and Fe^{2+} (*red dashed line*). *Plotted* data are shown as mean values with standard deviations from evaluations in six slices (and sample combination as described in the "Results" section)
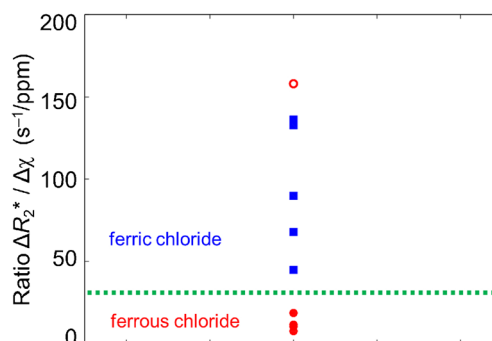

Fig. 4 Relaxation-to-susceptibility ratio $\Delta R_2^*/\Delta\chi$ of relaxation rate and susceptibility changes. The suggested threshold (*green dashed line*) for differentiation between ferric and ferrous chloride is 30 s^{-1}/ppm. The single data point with deviating behavior (*open circle*, 0.3 mmol/L ferrous chloride) is discussed in the main text; this data point has been included in all evaluations and also in the plots in Figs. 2 and 3

26]. On the other hand, both forms of iron similarly influence the magnetic susceptibility of the sample, which basically reflects the additional magnetic field of the paramagnetic iron ions (an effect that is widely independent of molecular dynamics and correlation times); the magnetic moments of ferrous and ferric ions are 4 μ_B (μ_B, Bohr magneton) and 5 μ_B, respectively [35], and hence of comparable magnitude. These different mechanisms responsible for relaxation changes on the one hand and susceptibility changes on the other hand can be exploited by determining the relaxation-to-susceptibility ratio $\Delta R_2^*/\Delta\chi$, which provides a good (and statistically significant) differentiation between both forms of iron ions. Thus, the change of iron concentration (independent of the oxidation state) can be determined quantitatively based on magnetic susceptibility differences and, simultaneously, ferric and ferrous iron ions can be differentiated based on MR relaxometry.

The iron distribution in the brain is on the verge to become an additional technique in the MRI-based diagnosis of neurodegenerative diseases such as PD and AD [36, 37]. Analogous to postmortem analysis of human brain tissue that shows a shift of the ratio of ferric to ferrous iron ions towards ferric iron ions [16], we showed in the present study that it is in principle possible not only to obtain MRI-based measurements of iron content in fluids but also to differentiate quantitatively between ferric and ferrous iron ions. We consider this work a first step in the assessment of shifts in ferric and ferrous iron ion ratios by MRI in vivo.

A consequence of our results is that MRI measurements of tissue iron concentrations based on relaxation effects (i.e., on the measurement of T_2^* or R_2^*) may require a particularly careful interpretation: When iron concentrations are quantified based on R_2^* values, the oxidation state of iron may also influence the relaxation rates in vivo and thus influence the reliability of the quantification.

To control systematic errors of our measurements, we prepared samples with HCl or sodium ascorbate added to the

ferric and ferrous chloride, respectively. Similar results for all our $FeCl_3$ measurements with and without HCl demonstrate that during the experiment no relevant amount of Fe^{3+} ions was extracted from the solution by the formation of $Fe(OH)_3$. Comparing Fe^{2+} samples with and without sodium ascorbate demonstrates that no relevant oxidation occurred during the experiments—if relevant oxidation had occurred, relaxation rates would have been expected to be substantially lower in the presence than in the absence of ascorbate. In contrast, the addition of deferoxamine to $FeCl_3$ solution resulted in a lower relaxation rate, since the interaction of water molecules and ferric ions can be expected to be reduced due to the chelation of the ions.

These observations justified the combination of the Fe^{3+} results with and without HCl as well as of the Fe^{2+} results with and without sodium ascorbate for quantitative analysis. This analysis resulted in a relaxivity (i.e., slope of the relaxation rate), which was about an order of magnitude (i.e., a factor of 16) higher (and significantly different) for Fe^{3+} than for Fe^{2+} ions. In contrast, the slopes of the susceptibility were similar for both forms of iron and only about 10% lower for Fe^{2+} than for Fe^{3+} (which is compatible with the small difference of the magnetic moments of both ions).

A limitation of our study is the occurrence of systematic errors in the individual results. These errors are caused predominantly by magnetic field inhomogeneities (visualized by the phase distribution in Fig. 1b and by the R_2^* variability in Fig. 5), which influence the accurate determination of both R_2^* and of the susceptibility, χ. In addition, the influence of low concentrations of iron (i.e., 0.1 or 0.3 mmol/L) on R_2^* and χ is small and therefore difficult to quantify. For instance, R_2^* relaxation rates between about 0.5 and 4 s^{-1} (corresponding to relaxation times between 250 and 2000 ms) are difficult to measure with feasible echo times between 10 and 80 ms. A consequence of these effects is large *relative* errors of the data points at low iron concentrations ($c_{Fe} \leq 0.3$ mmol/L). In particular, the visual outlier in Fig. 4 can be explained by an
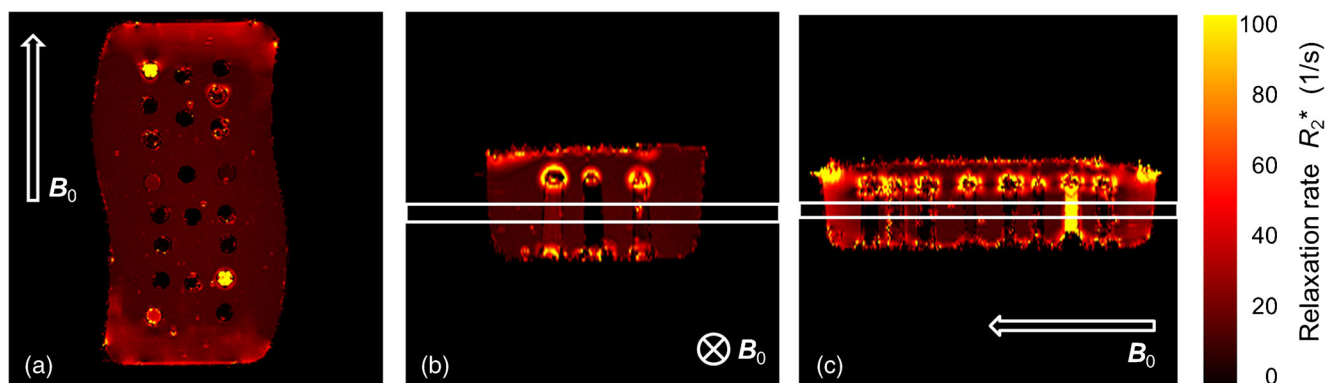
Fig. 5 R_2^* maps of the phantom **a** in coronal orientation (as acquired), **b** reformatted in axial orientation, and **c** reformatted in sagittal orientation. The *white arrows* indicate the B_0 magnetic field orientation. The position of the six central evaluated slices is shown as *white box* in **b** and **c**. These maps are meant as illustration of the R_2^* distribution in the phantom; the actual evaluation of R_2^* was not based on this map but was performed using the averaged signal intensities S(TE) in circular regions (in the six central slices) within each sample

incorrect systematic deviation towards too low values of the measured susceptibility of Fe^{2+} at a concentration of 0.3 mmol/L.

Conclusions

Ferrous and ferric chloride show significantly different relaxation behaviors in MRI but similar influences on the susceptibility. These properties can be used to differentiate ferrous and ferric samples in our phantom based on the relaxation-to-susceptibility ratio. Future work is required to investigate if this approach is also feasible for measurements of (changes of) Fe^{2+} and Fe^{3+} concentrations and of the ratio of Fe^{2+} to Fe^{3+} in biological tissue in vivo.

References

1. Singh N, Haldar S, Tripathi AK, Horback K, Wong J, Sharma D, Beserra A, Suda S, Anbalagan C, Dev S et al (2014) Brain iron homeostasis: from molecular mechanisms to clinical significance and therapeutic opportunities. Antioxid Redox Signal 20:1324–1363. doi:10.1089/ars.2012.4931

2. He N, Ling H, Ding B, Huang J, Zhang Y, Zhang Z, Liu C, Chen K, Yan F (2015) Region-specific disturbed iron distribution in early idiopathic Parkinson's disease measured by quantitative susceptibility mapping. Hum Brain Mapp 36:4407–4420. doi:10.1002/hbm.22928

3. Schweitzer AD, Liu T, Gupta A, Zheng K, Seedial S, Shtilbans A, Shahbazi M, Lange D, Wang Y, Tsiouris AJ (2015) Quantitative susceptibility mapping of the motor cortex in amyotrophic lateral sclerosis and primary lateral sclerosis. AJR Am J Roentgenol 204:1086–1092. doi:10.2214/AJR.14.13459

4. Dominguez JF, Ng AC, Poudel G, Stout JC, Churchyard A, Chua P, Egan GF, Georgiou-Karistianis N (2016) Iron accumulation in the basal ganglia in Huntington's disease: cross-sectional data from the IMAGE-HD study. J Neurol Neurosurg Psychiatry 87:545–549. doi:10.1136/jnnp-2014-310183

5. Belaidi AA, Bush AI (2016) Iron neurochemistry in Alzheimer's disease and Parkinson's disease: targets for therapeutics. J Neurochem 139(Suppl 1):179–197. doi:10.1111/jnc.13425

6. Schneider SA, Bhatia KP (2013) Excess iron harms the brain: the syndromes of neurodegeneration with brain iron accumulation (NBIA). J Neural Transm (Vienna) 120:695–703. doi:10.1007/s00702-012-0922-8

7. Popescu BF, George MJ, Bergmann U, Garachtchenko AV, Kelly ME, McCrea RP, Luning K, Devon RM, George GN, Hanson AD et al (2009) Mapping metals in Parkinson's and normal brain using rapid-scanning x-ray fluorescence. Phys Med Biol 54:651–663. doi:10.1088/0031-9155/54/3/012

8. Sian-Hulsmann J, Mandel S, Youdim MB, Riederer P (2011) The relevance of iron in the pathogenesis of Parkinson's disease. J Neurochem 118:939–957. doi:10.1111/j.1471-4159.2010.07132.x

9. Kostka M, Hogen T, Danzer KM, Levin J, Habeck M, Wirth A, Wagner R, Glabe CG, Finger S, Heinzelmann U et al (2008) Single particle characterization of iron-induced pore-forming alpha-synuclein oligomers. J Biol Chem 283:10992–11003. doi:10.1074/jbc.M709634200

10. Hillmer AS, Putcha P, Levin J, Hogen T, Hyman BT, Kretzschmar H, McLean PJ, Giese A (2010) Converse modulation of toxic alpha-synuclein oligomers in living cells by N'-benzylidene-benzohydrazide derivates and ferric iron. Biochem Biophys Res Commun 391:461–466. doi:10.1016/j.bbrc.2009.11.080

11. Wesemann W, Blaschke S, Solbach M, Grote C, Clement HW, Riederer P (1994) Intranigral injected iron progressively reduces striatal dopamine metabolism. J Neural Transm Park Dis Dement Sect 8:209–214

12. Logroscino G, Gao X, Chen H, Wing A, Ascherio A (2008) Dietary iron intake and risk of Parkinson's disease. Am J Epidemiol 168:1381–1388. doi:10.1093/aje/kwn273

13. Berg D (2007) Disturbance of iron metabolism as a contributing factor to SN hyperechogenicity in Parkinson's disease: implications for idiopathic and monogenetic forms. Neurochem Res 32:1646–1654. doi:10.1007/s11064-007-9346-5

14. Hallgren B, Sourander P (1958) The effect of age on the non-haemin iron in the human brain. J Neurochem 3:41–51

15. Zecca L, Gallorini M, Schunemann V, Trautwein AX, Gerlach M, Riederer P, Vezzoni P, Tampellini D (2001) Iron, neuromelanin and ferritin content in the substantia nigra of normal subjects at different ages: consequences for iron storage and neurodegenerative processes. J Neurochem 76:1766–1773

16. Sofic E, Riederer P, Heinsen H, Beckmann H, Reynolds GP, Hebenstreit G, Youdim MB (1988) Increased iron (III) and total iron content in post mortem substantia nigra of parkinsonian brain. J Neural Transm 74:199–205

17. Haacke EM, Cheng NY, House MJ, Liu Q, Neelavalli J, Ogg RJ, Khan A, Ayaz M, Kirsch W, Obenaus A (2005) Imaging iron stores in the brain using magnetic resonance imaging. Magn Reson Imaging 23:1–25. doi:10.1016/j.mri.2004.10.001

18. Langkammer C, Krebs N, Goessler W, Scheurer E, Ebner F, Yen K, Fazekas F, Ropele S (2010) Quantitative MR imaging of brain iron: a postmortem validation study. Radiology 257:455–462. doi:10.1148/radiol.10100495

19. Langkammer C, Krebs N, Goessler W, Scheurer E, Yen K, Fazekas F, Ropele S (2012) Susceptibility induced gray-white matter MRI contrast in the human brain. NeuroImage 59:1413–1419. doi:10.1016/j.neuroimage.2011.08.045

20. Uddin MN, Lebel RM, Wilman AH (2016) Value of transverse relaxometry difference methods for iron in human brain. Magn Reson Imaging 34:51–59. doi:10.1016/j.mri.2015.09.002

21. Kesavadas C, Santhosh K, Thomas B, Gupta AK, Kapilamoorthy TR, Bodhey N, Pendharker H, Patro S (2009) Signal changes in cortical laminar necrosis—evidence from susceptibility-weighted magnetic resonance imaging. Neuroradiology 51:293–298. doi:10.1007/s00234-009-0497-8

22. Rumzan R, Wang JJ, Zeng C, Chen X, Li Y, Luo T, Lv F, Wang ZP, Hou H, Huang F (2013) Iron deposition in the precentral grey matter in patients with multiple sclerosis: a quantitative study using

susceptibility-weighted imaging. Eur J Radiol 82:e95–e99. doi:10.1016/j.ejrad.2012.09.006

23. Xu X, Wang Q, Zhong J, Zhang M (2015) Iron deposition influences the measurement of water diffusion tensor in the human brain: a combined analysis of diffusion and iron-induced phase changes. Neuroradiology 57:1169–1178. doi:10.1007/s00234-015-1579-4

24. Liu M, Liu S, Ghassaban K, Zheng W, Dicicco D, Miao Y, Habib C, Jazmati T, Haacke EM (2016) Assessing global and regional iron content in deep gray matter as a function of age using susceptibility mapping. J Magn Reson Imaging 44:59–71. doi:10.1002/jmri.25130

25. Gore JC, Kang YS, Schulz RJ (1984) Measurement of radiation dose distributions by nuclear magnetic resonance (NMR) imaging. Phys Med Biol 29:1189–1197

26. Tokuhiro T, Appleby A, Leghrouz A, Metcalf R, Tokarz R (1996) Proton spin-lattice relaxation of water molecules in ferrous-ferric/agarose gel system. J Chem Phys 105:3761–3769. doi:10.1063/1.472196

27. Fricke H, Morse S (1927) The chemical action of roentgen rays on dilute ferrosulphate solutions as a measure of dose. Am J Roentgenol Radium Ther 18:430–432

28. Surry KJ, Austin HJ, Fenster A, Peters TM (2004) Poly(vinyl alcohol) cryogel phantoms for use in ultrasound and MR imaging. Phys Med Biol 49:5529–5546

29. Reinertsen I, Collins DL (2006) A realistic phantom for brain-shift simulations. Med Phys 33:3234–3240. doi:10.1118/1.2219091

30. Abdul-Rahman HS, Gdeisat MA, Burton DR, Lalor MJ, Lilley F, Moore CJ (2007) Fast and robust three-dimensional best path phase unwrapping algorithm. Appl Opt 46:6623–6635. doi:10.1364/AO.46.006623

31. Schweser F, Deistung A, Lehr BW, Reichenbach JR (2010) Differentiation between diamagnetic and paramagnetic cerebral lesions based on magnetic susceptibility mapping. Med Phys 37:5165–5178

32. Schweser F, Deistung A, Lehr BW, Reichenbach JR (2011) Quantitative imaging of intrinsic magnetic tissue properties using MRI signal phase: an approach to in vivo brain iron metabolism? NeuroImage 54:2789–2807. doi:10.1016/j.neuroimage.2010.10.070

33. de Rochefort L, Brown R, Prince MR, Wang Y (2008) Quantitative MR susceptibility mapping using piece-wise constant regularized inversion of the magnetic field. Magn Reson Med 60:1003–1009. doi:10.1002/mrm.21710

34. Clogg CC, Petkova E, Haritou A (1995) Statistical methods for comparing regression coefficients between models. Am J Sociol 100:1261–1293

35. Fulay PP (2010) Electronic, magnetic, and optical materials. CRC Press, Boca Raton, London, New York

36. Acosta-Cabronero J, Cardenas-Blanco A, Betts MJ, Butryn M, Valdes-Herrera JP, Galazky I, Nestor PJ (2017) The whole-brain pattern of magnetic susceptibility perturbations in Parkinson's disease. Brain 140:118–131. doi:10.1093/brain/aww278

37. van Bergen JM, Li X, Hua J, Schreiner SJ, Steininger SC, Quevenco FC, Wyss M, Gietl AF, Treyer V, Leh SE et al (2016) Colocalization of cerebral iron with amyloid beta in mild cognitive impairment. Sci Rep 6:35514. doi:10.1038/srep35514